Structured Singular Value Analysis of the VEGA Launcher in Atmospheric Flight

Pedro Simplício[a], Samir Bennani[b] and Xavier Lefort[c]
ESA - European Space Agency

Andrés Marcos[d]
University of Bristol

Christophe Roux[e]
ELV S.p.A.

Using the Structured Singular Value (SSV) μ, an independent control law assessment is presented for the VEGA launcher Thrust Vector Control (TVC) system. A systematic uncertainty modeling and analysis process is illustrated in order to retrieve and structure driving perturbation combinations affecting competing control system design requirements. It is demonstrated how μ analysis not only complements and generalises classical frequency domain stability assessments, but also how it applies naturally as a performance indicator to manage the requirements trade-off space. The proposed methodology is shown to be reliable and computationally more efficient than widespread verification and validation techniques that rely on random sampling via Monte Carlo analysis. Although not meant as a replacement of these traditional approaches, μ analysis effectively complements and enhances the verification and validation tasks by guiding the analyst towards worst-case convergence over the uncertain parameter search space. The attitude dynamics in atmospheric flight of Europe's lightweight VEGA launcher is assumed throughout the paper. Comparative robustness analysis results are shown between pre and post-flight assessments.

[a] GNC Systems Trainee, ESTEC GNC Section, Keplerlaan 1, 2201 AZ, Noordwijk, Netherlands.
[b] GNC Systems Eng., ESTEC GNC Section, Keplerlaan 1, 2201 AZ, Noordwijk, Netherlands, AIAA Senior Member.
[c] GNC Systems Eng., Directorate of Launchers VEGA Department, Via Galileo Galilei 64, 00044, Frascati, Italy.
[d] Senior Lecturer, Aerospace Eng. Department, University Walk, BS8 1TR, Clifton, UK, AIAA Senior Member.
[e] VEGA Control Eng., GNC Department, Corso Garibaldi 22, 00034, Colleferro, Italy, AIAA Senior Member.

Nomenclature

Variables:

C_{N_α}	Normalized lift (normal) force gradient (-), uncertainty level: [-60,+15]% (Mach$\leq$1) $\vee$ [-25,+8]% (Mach>1)
d	State of the delay model (-)
$\mathbf{d}_{\mathrm{x}}$	Reference and disturbance vector of system x (-)
D	Drag (axial) force (N), uncertainty level: [-35,+40]%
$\mathbf{e}_{\mathrm{x}}$	Performance output vector of system x (-)
$\mathcal{F}_{\mathrm{l}}, \mathcal{F}_{\mathrm{u}}$	Lower and upper LFT (-)
g	Gravitational acceleration (m/s^2)
$G(\mathrm{s})$	Generic system transfer function (-)
$H(\mathrm{s})$	Bending modes filter bench (-)
h	Altitude (m)
$I_{n\times n}$	Identity matrix of size n (-)
J_{y}	Lateral inertia moment of the launcher (kg.m^2), uncertainty level: transition from [-1,+1]% to [-5,+5]%
J_{N}	Lateral inertia moment of the nozzle (kg.m^2)
j	Imaginary unit (-)
K	Generic system steady-state gain (-)
$K(\mathrm{s})$	Flight controller transfer function (-)
$l_\alpha, l_{\mathrm{c}}, l_{\mathrm{N}}$	Aerodynamic, control and nozzle moment arm (m)
m	Total launcher mass (kg), uncertainty level: transition from [-0.1,+0.1]% to [-4,+4]%
m_{N}	Nozzle mass (kg)
$M(\mathrm{s}), N(\mathrm{s})$	Closed-loop transfer functions (-)
N_α	Lift (normal) force gradient (N/rad)
n_{w}	Wind model input signal (-)
$P(\mathrm{s})$	Plant transfer function (-)
Q	Dynamic pressure (Pa), uncertainty level: [-25,+30]%
q_{i}	Modal coordinate of bending mode i (-)
S	Launch vehicle reference area (m^2)
$S(\mathrm{s})$	Sensitivity transfer function (-)
s	Frequency domain operator, sometimes dropped for clarity (rad/s)
T	Thrust force (N), uncertainty level: [-10,+15]%
t	Flight time (s)
V	Launch vehicle airspeed (m/s), uncertainty level: [-8,+8]%
v_{w}	Wind speed (m/s)
$W(\mathrm{s})$	Weighting filter (-)

w_{x}	Relative uncertainty of variable x (-)
$\mathbf{w}_{\mathrm{x}}$, $\mathbf{z}_{\mathrm{x}}$	Uncertainty channel vectors of system x (-)
x	Longitudinal coordinate of the launcher body reference frame (m)
x_{CG}	Longitudinal center of gravity coordinate (m), uncertainty level: [-2,+2]%
x_{CP}	Longitudinal center of pressure coordinate (m), uncertainty level: [-25,+25]% (Mach$\leq$1) $\vee$ [-7,+7]% (Mach>1)
z	Launcher displacement with respect to the reference trajectory frame (m)
α	Angle of attack (rad)
β	TVC actuator deflection (rad)
δ_{x}	Parametric uncertainty of variable x (-)
Δ_{x}	Structured uncertainty of system x (-)
ζ_{i}	Damping ratio of bending mode i (-)
κ, λ	Imaginary and real component of the TVC LF mode (rad/s)
$\mu(M)$	Structured singular value of M (-)
$\mu_{\alpha}, \mu_{\mathrm{c}}$	Aerodynamic and control moment coefficient (s^{-2})
$\rho(M)$	Spectral radius of M (-)
σ_{i}	Rotation of bending mode i (rad), uncertainty level: [-50,+50]%
$\bar{\sigma}(M)$	Maximum singular value of M (-)
τ	Time delay (s), uncertainty level: [-40,+40]%
ϕ_{i}	Displacement of bending mode i (m), uncertainty level: [-50,+50]%
ψ	Pitch angle (rad)
ω	Angular frequency (rad/s)
ω_{i}	Eigenvalue frequency of bending mode i (rad/s), uncertainty level: [-20,+20]%

Subscripts:

BM	Relative to the launcher bending modes
BW	Bandwidth
c, $\hat{\mathrm{c}}$	Commands before and after actuation delay
critic	Critical perturbation
d	Relative to references and disturbances
e	Relative to parameter errors
HF, LF	High-frequency and low-frequency modes
i	Relative to the bending mode i
INS	Relative to the inertial navigation system position
L	Local-horizon reference frame
N	Relative to the nozzle center of gravity
NOM	Nominal value

MAX, MIN	Maximum/minimum value
P	Relative to the system plant
PVP	Relative to the TVC pivot point
Pz, Dz	Proportional and derivative drift control
Pψ, Dψ	Proportional and derivative attitude control
RB	Relative to the launcher rigid body
RP	For robust performance
SS	Steady-state component
TVC	Relative to the TVC model
u	Relative to the generalized uncertainty
w	Relative to the wind model
τ	Relative to the delay model

I. Introduction

The flight control of launch vehicles (LVs) is very challenging because, having the center of pressure located forward to the center of gravity, launchers are inherently unstable during atmospheric flight, which poses a high level of risk [1–3]. This risk is even more significant if there is a potential of interaction between low and high frequency dynamics. While loop gains are ideally as high as possible to improve aerodynamic performance, they have to be limited so as not to excite structural vibration and actuation modes. Furthermore, as the level of launcher modeling uncertainties is also high due to the lack of flight and experimental data, sufficient (robust) stability and performance margins must be ensured when designing the control system with respect to the ideal loop gains [3, 4].

The accurate determination of adequate stability margins, for a safe and robust flight, is therefore critical and entails extensive verification and validation (V&V) of the control system in closed-loop with high-fidelity vehicle models. In industry, stability and performance criteria are evaluated both for the nominal system and under dispersed parameter sets, which are typically injected through Monte Carlo (MC) campaigns or vertex approaches [4–6]. The MC method [5] consists in randomly sampling the system uncertain parameters followed by the assessment of the criteria associated to the requirements considered. On the other hand, the vertex approach [6] involves the verification of all the maximum/minimum combinations of parameters, also known as corner cases.

In both approaches, the most demanding sizing cases are determined from the direct inspection of the equations of motion. The validation procedures are then carried out either in the frequency domain, employing classical tools [2, 7] like Nichols plots from (analytically or numerically) linearized models of the equations, and in the time domain, using intrinsically complex nonlinear simulators.

Although being the state-of-practice in aerospace V&V, the methods mentioned above are limited in terms of a) reliability, as they offer few guarantees that the actual worst-case (WC) combinations of parameters (and thus robustness margins) are examined by the parameter sampling, b) efficiency, since the computational effort increases considerably with the dimension of parameters and samples analyzed (easily reaching several tens of thousands of simulations) and c) multi-channel understanding, as requirements have to be checked one at a time.

To overcome these limitations, advances have been exploited with the application of gradient-based, global and hybrid optimization algorithms for WC analysis [8, 9], searching the parameter space for a combination that minimises a certain cost function. Although these optimization-based approaches can typically identify criteria violation cases quickly, they are not systematic and the results are highly dependent on the problem and solver.

Furthermore, the application of analytical approaches such as the structured singular value μ have been considered in [10, 11]. This matrix measure was introduced in the 80s [12] and relies on models in the form of linear fractional transformations (LFTs) [13, 14]. It also comes together with valuable properties, such as the ability to manage complex uncertainties and the applicability not only for V&V, but also to provide relevant insights at design stage. In fact, μ analysis is developed under the post-modern $\mathcal{H}_\infty$ control framework [14], establishing a direct link with the most notable investigations on launcher robust control design throughout the past three decades [15–18].

In [11], a preliminary application of V&V μ analysis was introduced with a simple model of the VEGA launcher as case-study, being successfully compared to the outcomes of MC and optimization-based tools. VEGA is the European lightweight launch vehicle (LV) [19] developed under the responsibility of the European Space Agency (ESA) by ELV S.p.A. as the prime contractor. Having an in-orbit capability between 300 to 2500 kg, VEGA's reference mission is the delivery of a 1500 kg payload to a circular polar orbit at 700 km altitude. Its propulsion system is composed of three

solid propellant motors providing thrust for the first three stages (P80, Zefiro 23 and Zefiro 9) and a bi-propellant liquid engine for the upper module (AVUM). All the stages are controlled via a thrust vector control (TVC) system and also a roll and attitude control system (RACS) in the upper stage.

Motivated by the results of [11], the main goal of the present paper is to further demonstrate the potential of the structured singular value μ to provide a systematic way of finding the driving perturbation combinations of a system and its consequent degradations. With this objective in mind, the following major steps are conducted in this paper. First, the LFT modeling process of a generic launcher is detailed and adapted to the analysis of VEGA atmospheric flight. Key transfer functions of closed-loop launcher flight are also derived for the analytical assessment of common performance trade-offs. All the model parameters are taken from VEGA VV05 mission on June 23, 2015 [20] and most of them are time-varying. Then, the uncertain model is frozen at distinct instants of time and analyzed under nominal and dispersed configurations. The latter are assessed using μ analysis, from which WC conditions and parameter sensitivities are determined and linked to the nominal case through classical stability margins and performance indicators. This will establish the connection between post-modern control methodologies and classical frequency domain analysis. Finally, a clear interpretation of all the analysis outcomes is also provided and validated in the frequency domain, by checking against a MC campaign, and in the time domain, through high-fidelity simulations. Also, with VEGA being a production vehicle, pre and post-flight data is employed to support the whole analysis.

According to these steps, the paper is organized as follows. Section II presents the formulation of the problem and modeling approach addressed, which is then studied and arranged into a generalized structure for robustness assessment in Section III. The work continues with the nominal and robust stability (RS) analysis of the system in Section IV, which is then extended to incorporate robust performance (RP) criteria in Section V. In this section, the comparison with VEGA flight results is also included. The conclusions and recommendations of the paper are summarized in Section VI.

II. Problem and Model Description

This section begins with the summary of the necessary background on uncertainty modeling via linear fractional transformations (LFTs), followed by its application to describe the uncertain

atoms that are involved in the launch vehicle stability and performance assessment problem. In the end, the main launcher flight requirements considered during the analysis are also provided.

A. Uncertainty modeling approach

The stability and performance characteristics of any real system are affected by many dynamical perturbations (uncertainties), ranging from modeling inaccuracies (both deliberate and unknown) to external disturbances. Control systems are designed to work with a single nominal plant model, but a successful controller must function properly for all uncertainties within a bounded set [21].

As will become evident in the following subsections, the inaccurate knowledge of model parameters is the main source of uncertainty in launcher flight. In this paper, each parametric uncertainty x is modeled as an input multiplicative perturbation through the variation around its nominal value x_{NOM} of a certain relative range w_{x} (complex or real) as follows:

$$x = x_{\mathrm{NOM}} \left(1 + w_{\mathrm{x}} \delta_{\mathrm{x}}\right), \qquad \delta_{\mathrm{x}} \in [-1, 1] \tag{1}$$

This effect can also be written in the form of an LFT, following the conventional notation [13, 14]:

$$x = \mathcal{F}_{\mathrm{u}} \left\{ \begin{bmatrix} 0 & 1 \\ x_{\mathrm{NOM}} w_{\mathrm{x}} & x_{\mathrm{NOM}} \end{bmatrix}, \delta_{\mathrm{x}} \right\} \tag{2}$$

and every time x appears in a linear time-invariant (LTI) system, it can be replaced by Fig. 1.

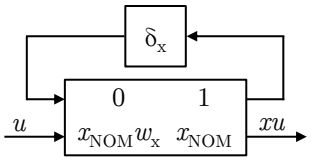

Fig. 1 LFT representation of an uncertain parameter

LFTs are particularly attractive for uncertainty representation due to their extreme modularity and because typical algebraic operations (e.g., inverse, cascade, parallel and feedback connections) preserve the LFT structure. Therefore, in an interconnected uncertain system, it is possible to isolate what is known and gather all the uncertainties into a perturbation block $\Delta_{\mathrm{x}} = \mathrm{diag}\left(\delta_{\mathrm{x}_1}, \delta_{\mathrm{x}_2}, ..., \delta_{\mathrm{x}_n}\right)$, $||\Delta_{\mathrm{x}}||_\infty \leq 1$. The general uncertainties at component level δ_{x_i} become then a block-diagonal structured perturbation Δ_{x} at interconnection level.

Nowadays, the process of pulling all the uncertainties out of an uncertain system can be automatically implemented using *MATLAB's Robust Control Toolbox*. For further details on this process, the reader is referred to [21].

In addition to these uncertainties, wind disturbances also play an important role in launcher dynamics, being responsible for the generation of aerodynamic loads and drift. For this reason, a wind model is also developed in Subsection II E and considered throughout the robustness assessment.

B. Launch vehicle model

For the robust stability and performance analysis, the motion of the LV is described by a bi-dimensional linear perturbation model, extensively found in the literature [22–25]. It is built by adding the contributions of the rigid body (RB) motion and the first four bending modes (BMs) of the LV, also accounting for wind disturbances, rigid damping and nozzle "tail wags dog" effects. Aero-elastic coupling effects are not taken into account in order to keep the complexity of the LFT system as low as possible.

This paper is focused on the atmospheric flight of VEGA, covering roughly the first 110 s of the mission, during which its first stage accelerates the launcher up to Mach 5.6. The RB model is schematized in Fig. 2 and implemented as follows:

$$\begin{bmatrix} \dot{z} \\ \ddot{z} \\ \dot{\psi} \\ \ddot{\psi} \end{bmatrix} = \begin{bmatrix} 0 & 1 & 0 & 0 \\ 0 & -\frac{N_\alpha}{mV} & \frac{D-T-N_\alpha}{m} & \frac{N_\alpha}{mV} l_\alpha \\ 0 & 0 & 0 & 1 \\ 0 & \frac{\mu_\alpha}{V} & \mu_\alpha & -\frac{\mu_\alpha}{V} l_\alpha \end{bmatrix} \begin{bmatrix} z \\ \dot{z} \\ \psi \\ \dot{\psi} \end{bmatrix} + \begin{bmatrix} 0 & 0 & 0 \\ -\frac{T}{m} & \frac{m_\mathrm{N}}{m} l_\mathrm{N} & \frac{N_\alpha}{mV} \\ 0 & 0 & 0 \\ -\mu_\mathrm{c} & \frac{m_\mathrm{N}}{J_\mathrm{y}} l_\mathrm{c} l_\mathrm{N} - \frac{J_\mathrm{N}}{J_\mathrm{y}} & -\frac{\mu_\alpha}{V} \end{bmatrix} \begin{bmatrix} \beta \\ \ddot{\beta} \\ v_\mathrm{w} \end{bmatrix} \tag{3}$$

$$\begin{bmatrix} \psi_\mathrm{INS} \\ \dot{z}_\mathrm{INS} \\ z_\mathrm{INS} \end{bmatrix} = \begin{bmatrix} 0 & 0 & 1 & 0 \\ 0 & 1 & 0 & x_\mathrm{CG} - x_\mathrm{INS} \\ 1 & 0 & x_\mathrm{CG} - x_\mathrm{INS} & 0 \end{bmatrix} \begin{bmatrix} z \\ \dot{z} \\ \psi \\ \dot{\psi} \end{bmatrix}$$

In Eq. (3), $[\psi_\mathrm{INS},\ \dot{z}_\mathrm{INS},\ z_\mathrm{INS}]^\mathrm{T}$ is the output vector at the inertial navigation system (INS) position x_INS, $N_\alpha = QSC_{\mathrm{N}_\alpha}$, $l_\alpha = x_\mathrm{CP} - x_\mathrm{CG}$, $l_\mathrm{c} = x_\mathrm{CG} - x_\mathrm{PVP}$, $l_\mathrm{N} = x_\mathrm{N} - x_\mathrm{PVP}$ and:

$$\mu_\alpha = \frac{N_\alpha}{J_\mathrm{y}} l_\alpha = \frac{QSC_{\mathrm{N}_\alpha}}{J_\mathrm{y}} l_\alpha \tag{4}$$

$$\mu_\mathrm{c} = \frac{T}{J_\mathrm{y}} l_\mathrm{c} \tag{5}$$

are the aerodynamic and control moment coefficients, representing the proneness of the vehicle to generate aerodynamic loads and its capacity to counteract them, shown in Fig. 3 over the flight.

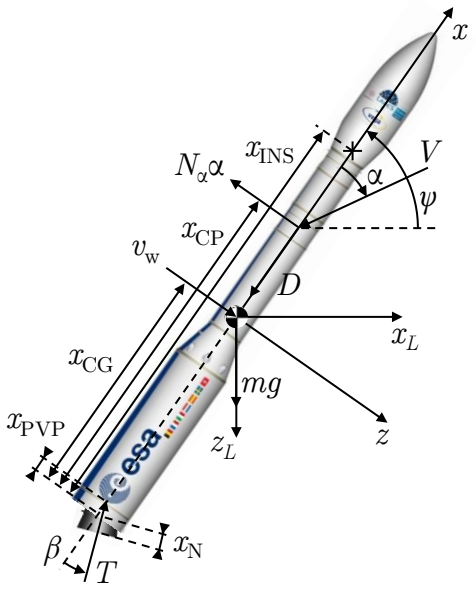

Fig. 2 Schematics of the rigid body model

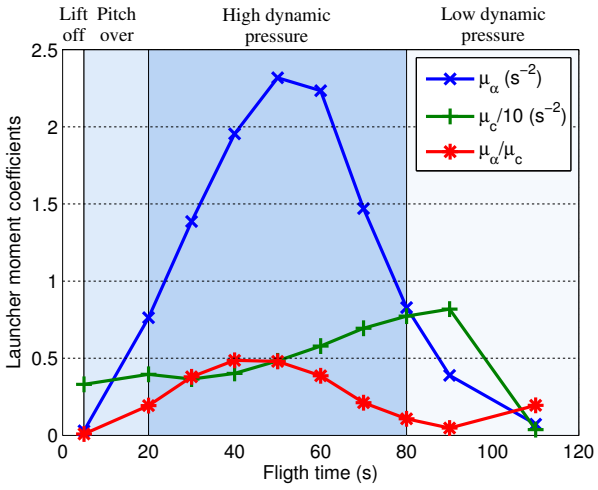

Fig. 3 Evolution of the aerodynamic and control moment coefficients over the flight

In this figure, μ_{c} is divided by 10 for visualization purposes and the ratio $\mu_\alpha/\mu_{\mathrm{c}}$ is critical for launcher control engineers. Under trim conditions, $\mu_\alpha/\mu_{\mathrm{c}} = \beta/\alpha$, where β and α are the trimming TVC deflection and angle of attack. In addition, the allowable TVC deflection must be enough to counteract wind gusts, effects of parameter variations and other disturbances. Thus, as observed from Fig. 3, the TVC system of VEGA is sized to enforce $\mu_\alpha/\mu_{\mathrm{c}} \leq 0.5$ throughout the flight and roughly proportional to the level of dynamic pressure. In addition, for a fixed launcher configuration, $\mu_\alpha\alpha$ depends only on $Q\alpha$, so this product is often used as an indicator of the aerodynamic load.

Parametric uncertainties are introduced in the system similarly to Subsection II A, resulting in the upper LFT $\mathcal{F}_{\mathrm{u}}\left\{G_{\mathrm{RB}}(\mathrm{s}),\, \Delta_{\mathrm{RB}}(\mathrm{s})\right\}$ with the uncertainty block:

$$\Delta_{\mathrm{RB}}(\mathrm{s}) = \mathrm{diag}\left(I_{4\mathrm{x}4}\delta_V, \delta_D, I_{2\mathrm{x}2}\delta_T, I_{3\mathrm{x}3}\delta_Q, I_{2\mathrm{x}2}\delta_{C_{\mathrm{N}\alpha}}, I_{4\mathrm{x}4}\delta_m, I_{5\mathrm{x}5}\delta_{J_{\mathrm{y}}}, I_{9\mathrm{x}9}\delta_{x_{\mathrm{CG}}}, I_{5\mathrm{x}5}\delta_{x_{\mathrm{CP}}}\right) \tag{6}$$

The LFT and its coverage in the frequency domain at t=60 s is provided in Fig. 4.

In addition, bending motion is modeled through the sum of the contributions of each bending mode (BM). These modes are sorted in ascending order of eigenvalue frequency and denoted BMi, $i = 1, 2, 3, 4$. The motion of each BM is approximated by a second-order system as follows [22, 25]:

$$\begin{aligned}
\begin{bmatrix} \dot{q}_{\mathrm{i}} \\ \ddot{q}_{\mathrm{i}} \end{bmatrix} &= \begin{bmatrix} 0 & 1 \\ -\omega_{\mathrm{i}}^2 & -2\zeta_{\mathrm{i}}\omega_{\mathrm{i}} \end{bmatrix} \begin{bmatrix} q_{\mathrm{i}} \\ \dot{q}_{\mathrm{i}} \end{bmatrix} + \begin{bmatrix} 0 & 0 & 0 \\ -T\phi_{\mathrm{i,PVP}} & J_{\mathrm{N}}\sigma_{\mathrm{i,INS}} + m_{\mathrm{N}}l_{\mathrm{N}}\phi_{\mathrm{i,PVP}} & 0 \end{bmatrix} \begin{bmatrix} \beta \\ \ddot{\beta} \\ v_{\mathrm{w}} \end{bmatrix} \\
\begin{bmatrix} \psi_{\mathrm{i,INS}} \\ \dot{z}_{\mathrm{i,INS}} \\ z_{\mathrm{i,INS}} \end{bmatrix} &= \begin{bmatrix} -\sigma_{\mathrm{i,INS}} & 0 \\ 0 & \phi_{\mathrm{i,INS}} \\ \phi_{\mathrm{i,INS}} & 0 \end{bmatrix} \begin{bmatrix} q_{\mathrm{i}} \\ \dot{q}_{\mathrm{i}} \end{bmatrix}
\end{aligned} \tag{7}$$

where q_{i} and $\dot{q}_{\mathrm{i}}$ are, respectively the modal coordinate of BMi and its time-derivative.

Parametric uncertainties are again introduced via upper LFTs $\mathcal{F}_{\mathrm{u}}\left\{G_{\mathrm{BMi}}(\mathrm{s}),\, \Delta_{\mathrm{BMi}}(\mathrm{s})\right\}$ for the two lower BMs, with the following structure for each mode:

$$\Delta_{\mathrm{BMi}}(\mathrm{s}) = \mathrm{diag}\left(I_{3\mathrm{x}3}\delta_{\omega_{\mathrm{i}}},\ \delta_T,\ \delta_{\phi_{\mathrm{i,PVP}}},\ \delta_{\sigma_{\mathrm{i,PVP}}},\ I_{2\mathrm{x}2}\delta_{\phi_{\mathrm{i,INS}}},\ \delta_{\sigma_{\mathrm{i,INS}}}\right) \tag{8}$$

The damping ratios are assumed to be known and equal to 0.008 and the uncertain eigenvalue frequencies are correlated using the disturbed variable $\omega_{\mathrm{BM}} \in [-1, 1]$ such that:

$$\omega_{\mathrm{i}} = \omega_{\mathrm{i,NOM}} + \frac{\omega_{\mathrm{BM}}}{2}(\omega_{\mathrm{i,MAX}} - \omega_{\mathrm{i,MIN}}) \tag{9}$$

The resulting uncertain system is depicted in Fig. 5.

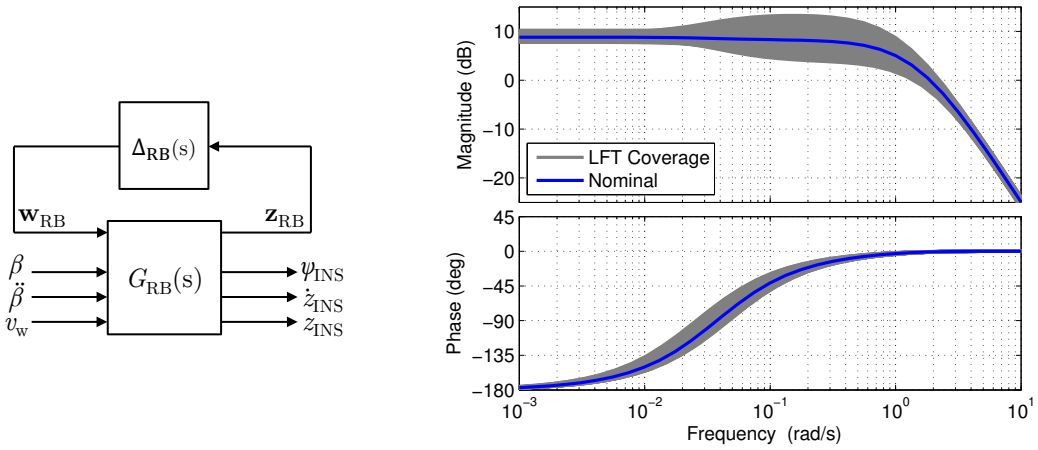

(a) Block diagram

(b) Frequency response $\psi_{\mathrm{INS}}(\mathrm{s})/\beta(\mathrm{s})$ at t=60 s

Fig. 4 Rigid body LFT model

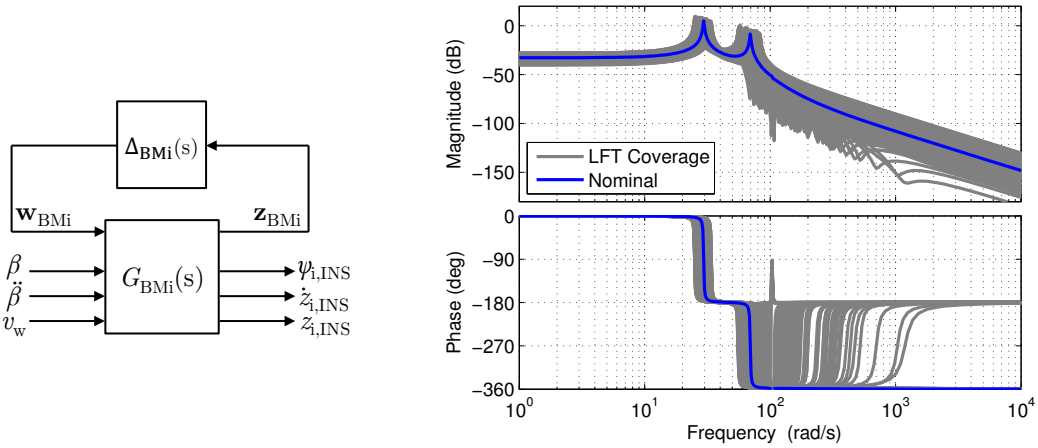

(a) Block diagram

(b) Frequency response $\sum \psi_{\mathrm{i,INS}}(\mathrm{s})/\beta(\mathrm{s})$ at t=60 s

Fig. 5 Bending modes LFT model

C. Actuation chain model

The actuation chain model is composed by the dynamics of the TVC actuator plus the effect of all the time delays that are originated by the hardware. TVC control is activated in the propeled

phase of flight, deflecting the nozzle along two directions via two electro-mechanical actuators and providing the desired thrust orientation. The TVC model is designed to fit the actuator responses obtained from hardware-in-the-loop simulations. It is characterized by second-order low-frequency (LF) and high-frequency (HF) complex modes. The LF mode, $G_{\mathrm{TVC_{LF}}}(\mathrm{s})$, is expressed as:

$$\begin{bmatrix} \dot{\beta} \\ \ddot{\beta} \end{bmatrix} = \begin{bmatrix} 0 & 1 \\ -\lambda^2 - \kappa^2 & 2\lambda \end{bmatrix} \begin{bmatrix} \beta \\ \dot{\beta} \end{bmatrix} + \begin{bmatrix} 0 \\ K_{\mathrm{TVC}}(\lambda^2 + \kappa^2) \end{bmatrix} \beta_{\hat{\mathrm{c}}} \tag{10}$$

in which $\beta_{\hat{\mathrm{c}}}$ is the commanded deflection and the position of the poles is modeled via a correlation between their real and imaginary parts, $\kappa = f(\lambda)$. The HF mode is represented by shaping an LTI uncertainty $\delta_{\mathrm{HF}}(\mathrm{s})$ around a nominal system $G_{\mathrm{TVC_{HF,NOM}}}(\mathrm{s})$, similarly to Eq. (1):

$$G_{\mathrm{TVC_{HF}}}(\mathrm{s}) = G_{\mathrm{TVC_{HF,NOM}}}(\mathrm{s})\left[1 + W_{\mathrm{TVC}}(\mathrm{s})\delta_{\mathrm{HF}}(\mathrm{s})\right] \tag{11}$$

The complete TVC dynamics is therefore given by:

$$\frac{\beta(\mathrm{s})}{\beta_{\hat{\mathrm{c}}}(\mathrm{s})} = G_{\mathrm{TVC}}(\mathrm{s}) = G_{\mathrm{TVC_{LF}}}(\mathrm{s})G_{\mathrm{TVC_{HF}}}(\mathrm{s}) \tag{12}$$

and the corresponding LFT $\mathcal{F}_{\mathrm{u}}\left\{G_{\mathrm{TVC}}(\mathrm{s}),\, \Delta_{\mathrm{TVC}}(\mathrm{s})\right\}$ and frequency response are shown in Fig. 6, where the uncertain block is:

$$\Delta_{\mathrm{TVC}}(\mathrm{s}) = \mathrm{diag}\left(I_{2\mathrm{x}2}\delta_{K_{\mathrm{TVC}}},\; I_{18\mathrm{x}18}\delta_{\lambda},\; I_{2\mathrm{x}2}\delta_{\mathrm{HF}}(\mathrm{s})\right) \tag{13}$$

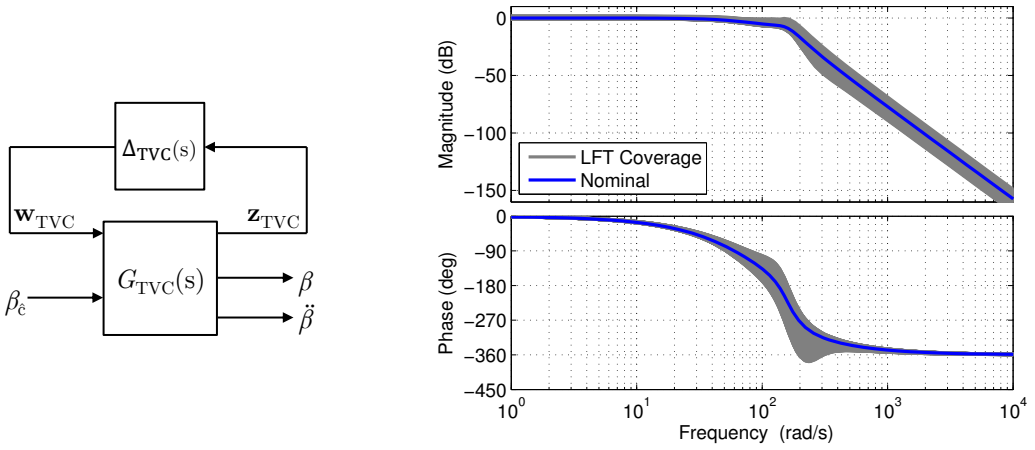

(a) Block diagram

(b) Frequency response $\beta(\mathrm{s})/\beta_{\hat{\mathrm{c}}}(\mathrm{s})$

Fig. 6 TVC LFT Model

The time delay τ of the actuation chain is also uncertain and modeled via $\mathcal{F}_{\mathrm{u}}\{G_\tau(\mathrm{s}),\, \Delta_\tau(\mathrm{s})\}$ (Fig. 7) through a second-order Padé approximation [21]:

$$\begin{bmatrix} \dot{d} \\ \ddot{d} \end{bmatrix} = \begin{bmatrix} 0 & 1 \\ -\dfrac{12}{\tau^2} & -\dfrac{6}{\tau} \end{bmatrix} \begin{bmatrix} d \\ \dot{d} \end{bmatrix} + \begin{bmatrix} 0 \\ -\dfrac{12}{\tau} \end{bmatrix} \beta_{\mathrm{c}} \qquad (14)$$

$$\beta_{\hat{\mathrm{c}}} = \dot{d} + \beta_{\mathrm{c}}$$

with the uncertain term:

$$\Delta_\tau(\mathrm{s}) = I_{4\mathrm{x}4}\delta_\tau \qquad (15)$$

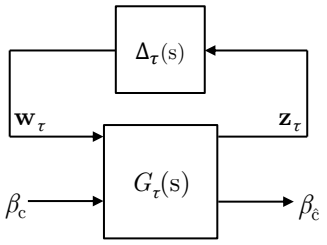

(a) Block diagram

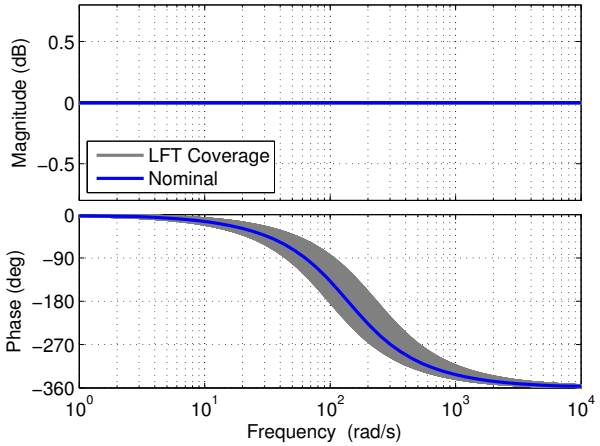

(b) Frequency response $\beta_{\hat{\mathrm{c}}}(\mathrm{s})/\beta_{\mathrm{c}}(\mathrm{s})$

Fig. 7 Time delay LFT model

D. Flight control system

The high-level objectives of the flight control system (and, indirectly, of the TVC system) are to manage, guide and control the launcher to achieve orbital conditions, keep the load levels limited in the face of control and external disturbances, optimize the trade-off between consumption, tracking and loads and perform the mission in a safe way in nominal and dispersed flight.

Each channel (pitch and yaw) has a proportional-derivative (PD) component for RB stability and performance with anti-drift control plus a numerically-optimized filter bench $H(\mathrm{s})$ to phase-stabilize the RB mode, notch the first BM and attenuate the upper modes [6, 19]. The channels are assumed uncoupled except in the presence of roll rate, when a compensation term is added. Being fed by the tracking error of ψ, $\dot{z}$ and z, each channel is described in the frequency domain as:

$$K(\mathrm{s},\mathrm{t}) = -\left[K_{\mathrm{P}\psi}(\mathrm{t}) + \mathrm{s}K_{\mathrm{D}\psi}(\mathrm{t}) \quad K_{\mathrm{D}z}(\mathrm{t}) \quad K_{\mathrm{P}z}(\mathrm{t})\right] H(\mathrm{s},\mathrm{t}) \tag{16}$$

The controller is discretized and all gains and filter coefficients are scheduled throughout the flight in order to cope with the time-varying system [19]. All the tunings are taken from VEGA VV05 mission. The scheduling parameter can be either non-gravitational velocity or time, which is the one assumed here, as evidenced in Eq. (16).

E. Wind model

For robust performance assessment, a wind generator is employed to model its impacts on the launcher. Based on aerospace guidelines [26], the wind generator is composed by an altitude-dependent steady-state profile with shear envelope $G_{\mathrm{w_{SS}}}(h)$ together with two Dryden filters to model the speed of wind gusts v_{w} from white noise with unitary variance n_{w}. The two filters, $G_{\mathrm{w_{LF}}}(h,\mathrm{s})$ and $G_{\mathrm{w_{HF}}}(h,\mathrm{s})$, are targeted at low-frequency/high-amplitude and high-frequency/low-amplitude gusts, respectively, and the wind model follows as:

$$\frac{v_{\mathrm{w}}(\mathrm{s})}{n_{\mathrm{w}}(\mathrm{s})} = G_{\mathrm{w}}(\mathrm{s}) = G_{\mathrm{w_{SS}}}(h) + G_{\mathrm{w_{LF}}}(h,\mathrm{s}) + G_{\mathrm{w_{HF}}}(h,\mathrm{s}) \tag{17}$$

The steady-state profile and Dryden filters are designed to cover the actual wind estimated from VEGA VV05 [20] flight data. The outcome of the wind model is illustrated in Fig. 8.

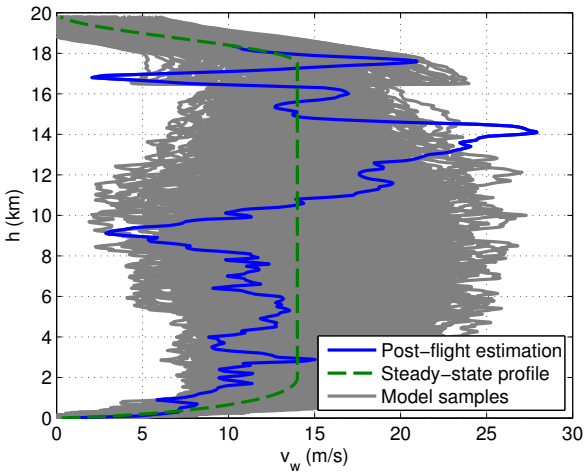

Fig. 8 Altitude profile of the wind model

F. Requirements formulation

Launcher missions impose a large set of challenges to the flight control system. While these are translated by a heavy set of nominal and dispersed requirements, the most relevant ones to have in mind for the following robustness analysis are listed below.

F1. Stability indicators: The aerodynamically unstable motion of the launcher shall be actively stabilized, while coping with the highly dynamical variation and uncertainty level of its parameters (Subsection II B). In addition, pre-specified gain margins (GM) and phase margins (PM) shall be ensured, as shown in Table 1. Phase margin requirements are formulated in terms of equivalent delay (i.e., phase over frequency ratio).

Table 1 VEGA Stability requirements

	Rigid body motion			Bending modes	
	LF GM	PM	HF GM	GM (if gain controlled)	PM (if phase controlled)
Nominal conditions	≥ 6 dB	≥ 100 ms	≤ -6 dB	≤ -3 dB	≥ 50 ms
Dispersed conditions	≥ 0.5 dB	≥ 40 ms	≤ -3 dB	≤ -3 dB	≥ 20 ms

F2. Attitude tracking: The attitude tracking error shall converge to zero in steady-state and the transient response shall be constrained in terms of maximum rate and overshoot. Closed-loop bandwidth shall therefore be high enough for proper tracking but sufficiently lower than BM1 to prevent flexible couplings.

F3. Load and drift management: On the one hand, induced aerodynamic loads shall be maintained below a required safety envelope (see Fig. 18b) by keeping the angle of attack small. On the other hand, the launcher lateral drift from its reference trajectory shall also be limited. This means that an optimized load vs. drift trade-off has to be achieved.

F4. Actuation minimization: The demanded TVC actuation during the flight shall never reach its deflection and bandwidth limits.

F5. Disturbance rejection: All parasitic effects shall be filtered out. These include not only external disturbances (e.g., wind), but also internal dynamics like BMs and pitch-yaw coupling

due to roll motion. As this filtering degrades the RB response properties, compensation shall be provided to recover rigid stability margins.

III. Generalized Structure for Analysis

With all the uncertain atoms and applicable requirements defined, the paper follows with their interconnection and transformation into a generalized structure for robustness analysis. Key transfer functions for closed-loop launcher flight are also derived and their relevance is highlighted.

A. Global uncertain model

The closed-loop system of the LV with the control law under analysis (Eq. (16)) is formed by connecting the blocks described in the previous section as depicted in Fig. 9.

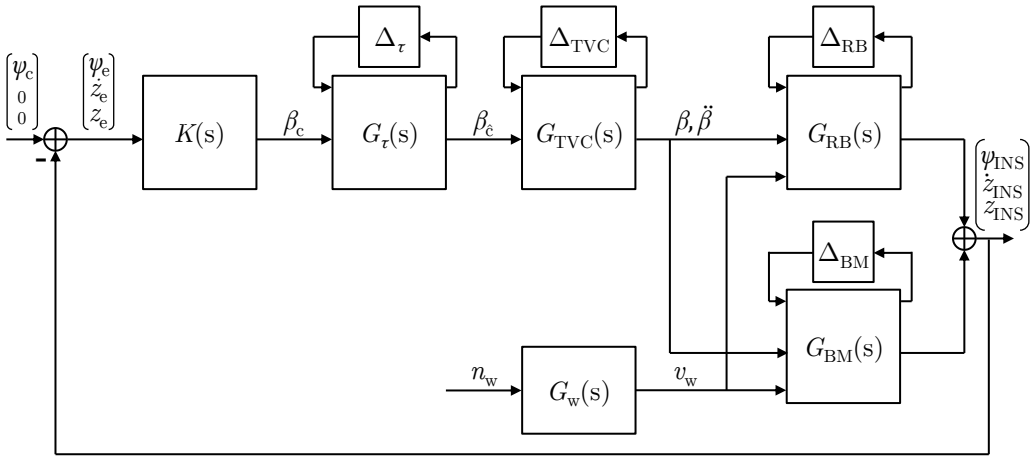

Fig. 9 Block diagram of the closed-loop system

A generic structure of the system is then obtained by rearranging the connections into an augmented LFT and extracting all the structured uncertainties in an orderly manner into the block $\Delta_{\mathrm{u}}(\mathrm{s}) = \mathrm{diag}(\Delta_{\mathrm{RB}}(\mathrm{s}),\ \Delta_{\mathrm{BM}}(\mathrm{s}),\ \Delta_{\mathrm{TVC}}(\mathrm{s}),\ \Delta_{\tau}(\mathrm{s}))$ with $||\Delta_{\mathrm{u}}(\mathrm{s})||_\infty \leq 1$, as indicated in Fig. 10.

In addition, key performance outputs are pulled out which, in this case, encompass not only the most relevant states of the launcher (ψ_{INS} and $\dot{z}_{\mathrm{INS}}$), but also the attitude error (ψ_{e}), actuation signal (β) and the indicator of the aerodynamic load level generated ($Q\alpha$). The different output channels are chosen based on the requirements of interest and can also be used at the control design stage.

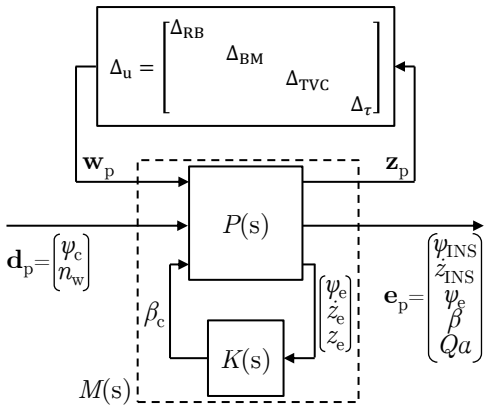

Fig. 10 Block diagram of the LFT model for robustness analysis

For analysis, as depicted in Fig. 10, it is convenient to absorb the loop between the controller and plant as a complex transfer matrix $M(\mathrm{s}) = \mathcal{F}_\mathrm{l}\left\{P(\mathrm{s}),\, K(\mathrm{s})\right\}$ such that:

$$\begin{bmatrix} \mathbf{z}_\mathrm{p}(\mathrm{s}) \\ \mathbf{e}_\mathrm{p}(\mathrm{s}) \end{bmatrix} = \begin{bmatrix} M_{11}(\mathrm{s}) & M_{12}(\mathrm{s}) \\ M_{21}(\mathrm{s}) & M_{22}(\mathrm{s}) \end{bmatrix} \begin{bmatrix} \mathbf{w}_\mathrm{p}(\mathrm{s}) \\ \mathbf{d}_\mathrm{p}(\mathrm{s}) \end{bmatrix} \tag{18}$$

in which $\mathbf{w}_\mathrm{p}(\mathrm{s})$ and $\mathbf{z}_\mathrm{p}(\mathrm{s})$ map the uncertainty channel, $\mathbf{d}_\mathrm{p}(\mathrm{s}) = [\psi_\mathrm{c}(\mathrm{s}),\, n_\mathrm{w}(\mathrm{s})]^\mathrm{T}$ represents the attitude reference and wind disturbance signals and $\mathbf{e}_\mathrm{p}(\mathrm{s}) = [\psi_\mathrm{INS}(\mathrm{s}),\, \dot{z}_\mathrm{INS}(\mathrm{s}),\, \psi_\mathrm{e}(\mathrm{s}),\, \beta(\mathrm{s}),\, Q\alpha(\mathrm{s})]^\mathrm{T}$ is the performance output vector. Following this framework [13, 14], the relationship between reference/disturbance and performance signals is provided by the upper LFT of $M(\mathrm{s})$ and $\Delta_\mathrm{u}(\mathrm{s})$:

$$\mathbf{e}_\mathrm{p}(\mathrm{s}) = \mathcal{F}_\mathrm{u}\left\{M(\mathrm{s}),\, \Delta_\mathrm{u}(\mathrm{s})\right\}\mathbf{d}_\mathrm{p}(\mathrm{s}) \tag{19}$$

$$\mathcal{F}_\mathrm{u}\left\{M(\mathrm{s}),\, \Delta_\mathrm{u}(\mathrm{s})\right\} = M_{22}(\mathrm{s}) + M_{21}(\mathrm{s})\Delta_\mathrm{u}(\mathrm{s})\left(I_{nxn} - M_{11}(\mathrm{s})\Delta_\mathrm{u}(\mathrm{s})\right)^{-1} M_{12}(\mathrm{s}) \tag{20}$$

where both $M(\mathrm{s})$ and $\Delta_\mathrm{u}(\mathrm{s})$ are assumed stable, which is ensured through the proper design of $K(\mathrm{s})$.

Equation (20) clearly shows that the output of the system is affected by its nominal response $M_{22}(\mathrm{s})$ (for $\Delta_\mathrm{u}(\mathrm{s}) = 0$) plus the effect of $\Delta_\mathrm{u}(\mathrm{s})$. Furthermore, even with a stable nominal system, the stability of the LFT depends directly on the existence of $\left(I_{nxn} - M_{11}(\mathrm{s})\Delta_\mathrm{u}(\mathrm{s})\right)^{-1}$. This means that the condition for robust stability, i. e., that the controller $K(\mathrm{s})$ ensures stability for all plants in the uncertainty set, is only influenced by the channel from $\mathbf{w}_\mathrm{p}(\mathrm{s})$ to $\mathbf{z}_\mathrm{p}(\mathrm{s})$ and corresponds to:

$$\det\left(I_{nxn} - M_{11}(\mathrm{s})\Delta_\mathrm{u}(\mathrm{s})\right) \neq 0, \qquad \forall\Delta_\mathrm{u}(\mathrm{s}) : ||\Delta_\mathrm{u}(\mathrm{s})||_\infty \leq 1 \tag{21}$$

While this condition is assessed in Section IV, the rest of this section is focused on the nominal response of the system.

B. Classical closed-loop indicators

As mentioned in the previous subsection, the nominal performance (without uncertainties) of the closed-loop system is directly analyzed through the individual responses of $M_{22}(\mathrm{s})$. In order to perform this assessment analytically, this subsection assumes: no rigid damping ($l_\alpha/V \approx 0$), no "tail wags dog" effects ($m_\mathrm{N}/m \approx 0$ and $J_\mathrm{N}/J_\mathrm{y} \approx 0$), no bending motion or filters ($q_\mathrm{i}, \dot{q}_\mathrm{i} \approx 0$ and $H(\mathrm{s}) \approx I_{3\mathrm{x}3}$), no TVC dynamics or delays ($\beta \approx \beta_{\hat{\mathrm{c}}} \approx \beta_\mathrm{c}$), no offset between center of gravity (CG) and INS ($x_\mathrm{CG} - x_\mathrm{INS} \approx 0$) and no proportional drift control ($K_{\mathrm{P}z} \approx 0$). The analytical assessment is presented exclusively in this subsection to provide a better understanding of the problematic; therefore, none of these assumptions are applicable to the rest of the work in the paper.

Following the assumptions above, the transfer functions from attitude commands ψ_c and wind gusts v_w to the launcher attitude ψ and drift rate $\dot{z}$ are determined from the system:

$$\begin{bmatrix} \mathrm{s}^2 + \mu_\mathrm{c} K_{\mathrm{D}\psi}\mathrm{s} + \mu_\mathrm{c} K_{\mathrm{P}\psi} - \mu_\alpha & \mu_\mathrm{c} K_{\mathrm{D}z} - \dfrac{\mu_\alpha}{V} \\ TK_{\mathrm{D}\psi}\mathrm{s} + T\left(K_{\mathrm{P}\psi}+1\right) + N_\alpha - D & m\mathrm{s} + TK_{\mathrm{D}z} + \dfrac{N_\alpha}{V} \end{bmatrix} \begin{bmatrix} \psi(\mathrm{s}) \\ \dot{z}(\mathrm{s}) \end{bmatrix} = \begin{bmatrix} \mu_\mathrm{c} K_{\mathrm{D}\psi}\mathrm{s} + \mu_\mathrm{c} K_{\mathrm{P}\psi} \\ TK_{\mathrm{D}\psi}\mathrm{s} + TK_{\mathrm{P}\psi} \end{bmatrix} \psi_\mathrm{c}(\mathrm{s}) + \begin{bmatrix} -\dfrac{\mu_\alpha}{V} \\ \dfrac{N_\alpha}{V} \end{bmatrix} v_\mathrm{w}(\mathrm{s}) \tag{22}$$

With characteristic polynomial given by:

$$\begin{aligned} c(\mathrm{s}) = m\mathrm{s}^3 + \left[TK_{\mathrm{D}z} + m\mu_\mathrm{c} K_{\mathrm{D}\psi} + \frac{N_\alpha}{V}\right]\mathrm{s}^2 + \left[m\left(\mu_\mathrm{c} K_{\mathrm{P}\psi} - \mu_\alpha\right) + \frac{K_{\mathrm{D}\psi}}{V}\left(\mu_\mathrm{c} N_\alpha + \mu_\alpha T\right)\right]\mathrm{s} + \\ + \mu_\mathrm{c}\left(K_{\mathrm{P}\psi}\frac{N_\alpha}{V} - K_{\mathrm{D}z}(T + N_\alpha - D)\right) + \mu_\alpha\left(\frac{T(K_{\mathrm{P}\psi}+1) - D}{V} - TK_{\mathrm{D}z}\right) \end{aligned} \tag{23}$$

the solutions of Eq. (22) correspond to:

$$\frac{\psi(\mathrm{s})}{\psi_\mathrm{c}(\mathrm{s})} = \frac{1}{c(\mathrm{s})}\left\{m\mu_\mathrm{c} K_{\mathrm{D}\psi}\mathrm{s}^2 + \left[m\mu_\mathrm{c} K_{\mathrm{P}\psi} + \frac{K_{\mathrm{D}\psi}}{V}\left(\mu_\mathrm{c} N_\alpha + \mu_\alpha T\right)\right]\mathrm{s} + \frac{K_{\mathrm{P}\psi}}{V}\left(\mu_\mathrm{c} N_\alpha + \mu_\alpha T\right)\right\} \tag{24}$$

$$\begin{aligned} \frac{\dot{z}(\mathrm{s})}{\psi_\mathrm{c}(\mathrm{s})} = \frac{1}{c(\mathrm{s})}\left\{TK_{\mathrm{D}\psi}\mathrm{s}^3 + TK_{\mathrm{P}\psi}\mathrm{s}^2 - K_{\mathrm{D}\psi}\left[\mu_\mathrm{c}\left(T + N_\alpha - D\right) + \mu_\alpha T\right]\mathrm{s} - \right. \\ \left. - K_{\mathrm{P}\psi}\left[\mu_\mathrm{c}\left(T + N_\alpha - D\right) + \mu_\alpha T\right]\right\} \end{aligned} \tag{25}$$

$$\frac{\psi(\mathrm{s})}{v_\mathrm{w}(\mathrm{s})} = -\frac{1}{Vc(\mathrm{s})}\left\{m\mu_\alpha\mathrm{s} + K_{\mathrm{D}z}\left(\mu_\mathrm{c} N_\alpha + \mu_\alpha T\right)\right\} \tag{26}$$

$$\frac{\dot{z}(\mathrm{s})}{v_\mathrm{w}(\mathrm{s})} = \frac{1}{Vc(\mathrm{s})}\left\{N_\alpha\mathrm{s}^2 + K_{\mathrm{D}\psi}\left(\mu_\mathrm{c} N_\alpha + \mu_\alpha T\right)\mathrm{s} + \mu_\mathrm{c} N_\alpha K_{\mathrm{P}\psi} + \mu_\alpha\left[T(K_{\mathrm{P}\psi}+1) - D\right]\right\} \tag{27}$$

The remaining performance outputs can then be determined from:

$$\psi_{\mathrm{e}}(\mathrm{s}) = \psi_{\mathrm{c}}(\mathrm{s}) - \psi(\mathrm{s}) \tag{28}$$

$$\beta(\mathrm{s}) = -\left(K_{\mathrm{P}\psi} + \mathrm{s}K_{\mathrm{D}\psi}\right)\left(\psi_{\mathrm{c}}(\mathrm{s}) - \psi(\mathrm{s})\right) + K_{\mathrm{D}z}\dot{z}(\mathrm{s}) \tag{29}$$

$$Q\alpha(\mathrm{s}) = Q\left(\psi(\mathrm{s}) + \frac{\dot{z}(\mathrm{s}) - v_{\mathrm{w}}(\mathrm{s})}{V}\right) \tag{30}$$

These transfer functions are extremely important as they allow to study basic classical properties of the system (e.g., cross-over frequency, overshoots and limits when $\mathrm{s} \to 0$ or $\mathrm{s} \to \infty$) at control interpolation conditions and thus to analytically budget all the trade-offs between them that might be required. Of particular relevance is the sensitivity function $S(j\omega) = \psi_{\mathrm{c}}(j\omega)/\psi_{\mathrm{e}}(j\omega)$, from ψ_{c} to ψ_{e}, as it provides a direct indication of the minimum attainable stability margins through [2]:

$$\mathrm{GM} \geq \frac{||S(j\omega)||_\infty}{||S(j\omega)||_\infty - 1} \tag{31}$$

$$\mathrm{PM} \geq 2\arcsin\left(\frac{1}{2\,||S(j\omega)||_\infty}\right) \tag{32}$$

where $||S(j\omega)||_\infty$ is the amplitude peak of the sensitivity transfer function $S(j\omega)$, which is depicted in Fig. 11.

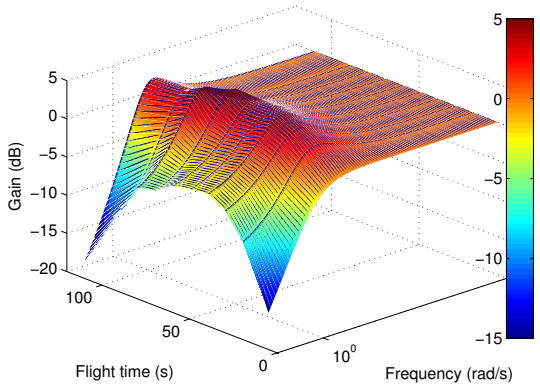

Fig. 11 Amplitude of the sensitivity function $S(j\omega)$ over the flight

As shown in the figure, the high dynamic pressure region (between 50 and 60 s) has an adverse effect on the overall system stability, with a sensitivity peak roughly 3 dB higher in this zone that indicates smaller gain and phase margins. Here, $K_{\mathrm{D}z}$ is set to 0 in order to assess the sensitivity of the system without drift control, allowing to map the RB performance objectives upon design.

Also, as bending motion was neglected for this analysis, the sensitivity function of Fig. 11 captures only effects of the rigid body. For the remainder of the paper, without these assumptions, the actual system sensitivity is further degraded, as explained in Subsection II F.

It shall also be highlighted that control tunings are fixed to those of VEGA VV05 mission for all the assessments throughout the following sections. Moreover, these assessments are completely independent of the methods employed for control design.

IV. Robust Stability Assessment

This section is aimed at illustrating the stability assessment process, from the analysis of the nominal system using classical control tools to the robustness insights provided via the structured singular value μ, showing how the stability indicators highlighted in Subsection II F are degraded in the presence of system uncertainties.

A. Classical stability margins analysis

Under nominal state, the necessary condition for system stability is simply to have all the closed-loop poles in the left side of the complex plane. In this case, levels of stability can be assessed using classical indicators (e.g., gain and phase margins) and tools such as Nyquist and Nichols plots [2, 7]. As introduced in Subsection II F1, the most relevant stability indicators for LV flight [17] include (in ascending order of frequency): 1) rigid body LF gain margin (LF GM), 2) rigid body phase margin (PM) and equivalent delay, 3) rigid body HF gain margin (HF GM), 4) first phase margin of BM1 (PM1), 5) gain peak of BM1 (Pk1), 6) second phase margin of BM1 (PM2) and 7) gain peak of BM2 (Pk2). All these indicators are highlighted in Fig. 12a, which represents the Nichols chart of the closed-loop attitude channel at distant instant over the flight, from t=5 s to t=110 s.

For the rigid mode, the stability margins at each instant are gathered in Fig. 12b, where phase margin is reported in terms of the equivalent delay to match the requirements formulation (Subsection II F1). These results confirm that system stability under nominal conditions is ensured throughout the flight, although with narrower stability margins when aerodynamic loads become more intense. Nevertheless, for the nominal system, RB margins are always larger 6.4 dB gain and 131 ms delay.

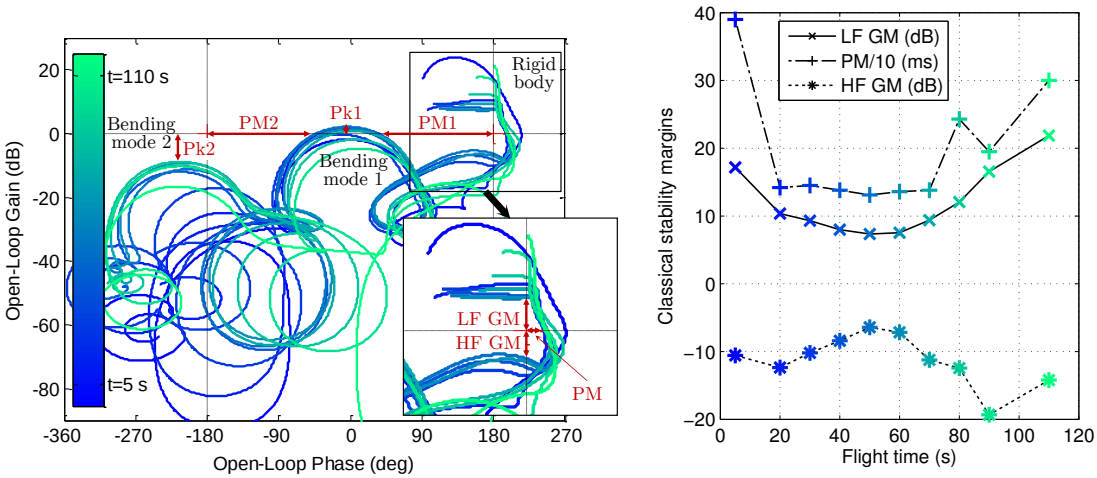

(a) Nominal Nichols charts $\psi_{\text{INS}}(\text{s})/\psi_{\text{e}}(\text{s})$

(b) RB stability margins

Fig. 12 Classical stability analysis over the flight

B. Stability μ analysis

As introduced in Subsection III A, in the presence of uncertainties, robust stability (RS) of the system is determined if it is nominally stable and the existence of $(I - M_{11}(\text{s})\Delta_{\text{u}}(\text{s}))^{-1}$ is ensured. This is assessed by the structured singular value $\mu_{\Delta_{\text{u}}}(M_{11})$, defined as [11–14]:

$$\mu_{\Delta_{\text{u}}}(M_{11}) = \frac{1}{\min_{\Delta_{\text{u}}} \{\bar{\sigma}(\Delta_{\text{u}}) : ||\Delta_{\text{u}}||_\infty \leq 1, \det(I - M_{11}\Delta_{\text{u}}) = 0\}} \tag{33}$$

In this expression, M_{11} is a complex matrix, Δ_{u} is a set of real and/or complex matrices with a given block diagonal structure, $\mu_{\Delta_{\text{u}}}(M_{11})$ is zero if no structured Δ_{u} exists and $\mu_{\Delta_{\text{u}}}(M_{11}) \in \mathbb{R}^+$ otherwise. Following this definition and assuming that the nominal system $M(\text{s})$ and perturbation vector $\Delta_{\text{u}}(\text{s})$ are stable, the system $\mathcal{F}_{\text{u}}\{M(\text{s}), \Delta_{\text{u}}(\text{s})\}$ is stable over all allowable uncertain elements ($||\Delta_{\text{u}}(\text{s})||_\infty \leq 1$) if and only if [12, 14]:

$$\mu_{\Delta_{\text{u}}}(M_{11}(j\omega)) < 1, \quad \forall \omega \in \mathbb{R} \tag{34}$$

Moreover, the norm of the smallest set of uncertainties that destabilises the system is given by $||\mu_{\Delta_{\text{u}}}(M_{11}(j\omega))||_\infty^{-1}$. Due to its non-convex character, $\mu_{\Delta_{\text{u}}}(M_{11})$ cannot be calculated directly, so μ algorithms determine lower and upper bounds of the structured singular value, such that:

$$\max_{Q \in \mathbf{Q}} \rho(QM_{11}) \leq \mu_{\Delta_{\text{u}}}(M_{11}) \leq \inf_{D \in \mathbf{D}} \bar{\sigma}(DM_{11}D^{-1}) \tag{35}$$

where Q and D are matrices from two complex subsets $\mathbf{Q}$ and $\mathbf{D}$ defined to get the bounds as close as possible [13], ρ indicates the spectral radius of the matrix and $\bar{\sigma}$ its maximum singular value. For more accurate bounds, the size of LFT models shall be kept as small as possible while capturing the most relevant physical phenomena of the real system and their interplay with the uncertainties.

Figure 13 shows four visualizations of the robust stability results, in which $\mu_{\Delta_u}(M_{11})$ bounds are computed using *MATLAB's Robust Control Toolbox* [21] after constructing the closed-loop system at distinct instants of time. Results are depicted up to 40 rad/s as the analysis is focused on the rigid body motion and first bending mode. The analysis is made directly with frequency response data (continuous plant and discrete controller) to avoid unnecessary conversions. M_{11} is taken as defined in Eq. (18) and Δ_u corresponds to the uncertainty of Fig. 10. As it is known that less accurate lower bounds are obtained when the block structure of Δ_u includes pure reals [14], small complex terms (up to 5%) were introduced in the uncertain perturbations. This addition of non-physical uncertainty is also reflected into a slightly more conservative lower bound of $\mu_{\Delta_u}(M_{11})$.

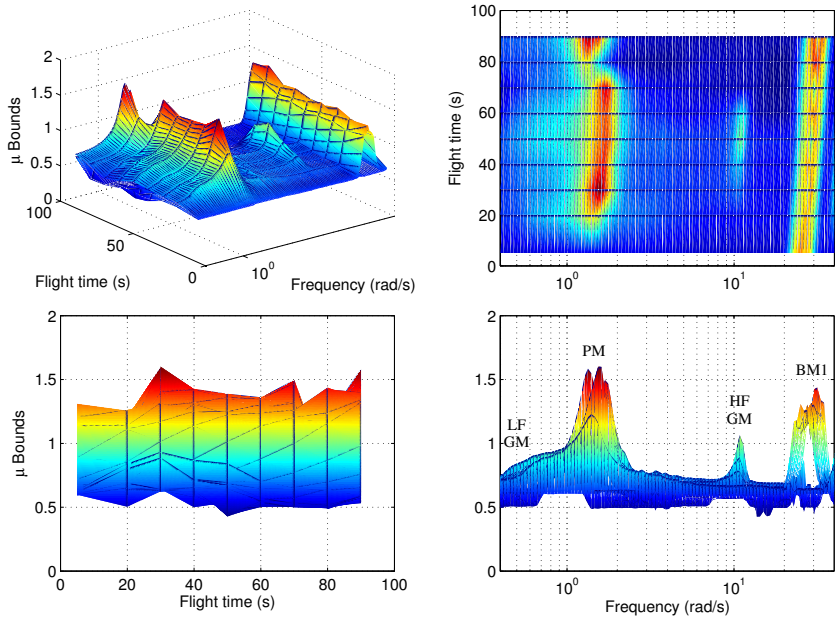

Fig. 13 Robust stability results over the flight

The μ plot clearly shows the critical areas identified in Fig. 12a over the frequency, most notably the surroundings of LF GM, PM, HF GM and BM1. In each frequency zone, stability degradation is achieved by shifting the Nichols plot in the direction of the instability point. Therefore, the μ plot

gives a frequency-wise insight on how stability margins are affected. In accordance to this, stability degradation is associated to a phase loss around PM frequency, gain increase for HF GM and phase shift of the two BM1 crossings towards instability.

The temporal variation of robust stability through the flight is perceived by freezing the system and executing local μ tests at different interpolation points in time. Figure 13 highlights particularly the degradation of HF GM with the intensification of aerodynamic loads (Fig. 12b) and the frequency increase of BM1 as a consequence of propellant burn. The extrapolation based on local μ analyses is actually an approximation of the global behavior of the LFT. Alternatively, advanced linear parameter-varying (LPV) techniques [27] can be employed for the full parametrization of the system.

A more detailed μ analysis is now provided, focused on the system configuration at t=60 s (high dynamic pressure region), with Fig. 14 representing the slice of the system μ plot at this instant.

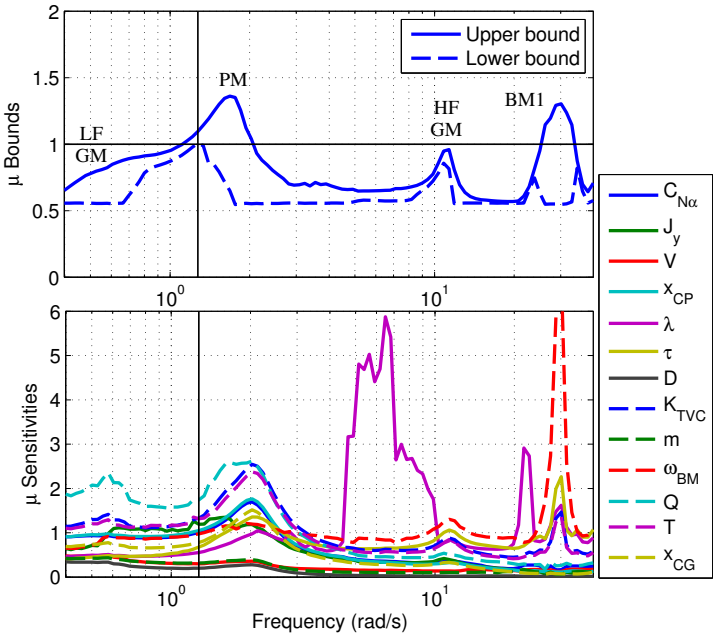

Fig. 14 Robust stability results at t=60 s

The uppermost plot shows in detail the bounds of $\mu_{\Delta_u}(M_{11})$ over frequency. It shows also that there is a peak (around 1.3 rad/s) where both bounds are above 1, anticipating that the system is not robustly stable. In other words, there is at least a combination of parameters $\Delta_{u_{critic}}(s)$ within the allowable uncertainty set, i.e., with size $||\Delta_{u_{critic}}(s)||_\infty = ||\mu_{\Delta_u}(M_{11})||_\infty^{-1} \leq 1$, that makes it unstable. This conclusion is of course not acceptable for a launch vehicle and has been fed into the

review of VEGA's stability requirements. It is also interesting to notice that there are two lower bound peaks for BM1, which represent the reduction of the two distinct phase margins of this mode (PM1 and PM2, in Fig. 12a).

The second plot introduces information about the sensitivity of μ with respect to each uncertain parameter, i.e., $\partial\bar{\sigma}(DM_{11}D^{-1})/\partial\delta_{\mathrm{i}}$. For clarity, some of the parameters (ϕ_{i}, σ_{i} and δ_{HF}) are not represented. The μ sensitivity is extremely useful to identify which uncertain parameters have more impact in the solution of μ over the frequency and therefore validate the meaningfulness of the results obtained, supporting or complementing considerations derived from an engineering perspective.

In accordance with this, the sensitivity plot shows the existence of a LF zone (around PM frequency) mostly impacted by parameters related to the slow dynamics of the system, such as dynamic pressure Q, thrust T, inertia J_{y} and TVC gain K_{TVC}, as well as an HF zone (around BM1 frequency) where the solution is determined by high-frequency parameters, mainly the BM frequency ω_{BM}, time delay τ and TVC bandwidth λ. As mentioned in Subsection II F, enough separation shall be provided between these two zones to avoid undesirable couplings. The sensitivity peak between PM and HF GM shows also that the system stability is strongly influenced by the TVC behavior, meaning that it shall be accurately modeled, in particular around these critical frequencies.

In addition, it is possible to extract the perturbation vector $\Delta_{\mathrm{u}}(\mathrm{s})$ that generates each value of μ. As the structured singular value is an indicator of stability degradation in the presence of uncertainties, the information it provides is extremely valuable for the identification of the worst-case (WC) response degradation [11]. The WC perturbation $\Delta_{\mathrm{u_{critic}}}(\mathrm{s})$ is thus the one that corresponds to the peak of μ. Furthermore, the WC closed-loop system is constructed as $\mathcal{F}_{\mathrm{u}}\left\{M(\mathrm{s}),\, \Delta_{\mathrm{u_{critic}}}(\mathrm{s})\right\}$ and its stability properties may be analyzed as before. The comparison between nominal and WC response from the lower bound of μ is illustrated in Fig. 15a.

Although instability of the WC system is not visible in the Nichols chart of Fig. 15a due to its numerical inaccuracies, at least one of the closed-loop poles is about to cross the imaginary axis for the combination of uncertainties found via μ analysis. As depicted, this combination generates in fact a significant degradation of the system response in the LF area, with a critical reduction of gain and delay stability margins to 2.1 dB and 115 ms, respectively.

The same approach allows to determine the WC stability margins for other instants of time, which are plotted against the nominal ones of Fig. 12b in Fig. 15b. Similarly to what is shown in Fig. 15a for t=60 s, the WC conditions found with μ lead to a considerable reduction of LF GM and also PM throughout the flight and to the consequent (negative) increase of HF GM as the Nichols plot is essentially shifted down.

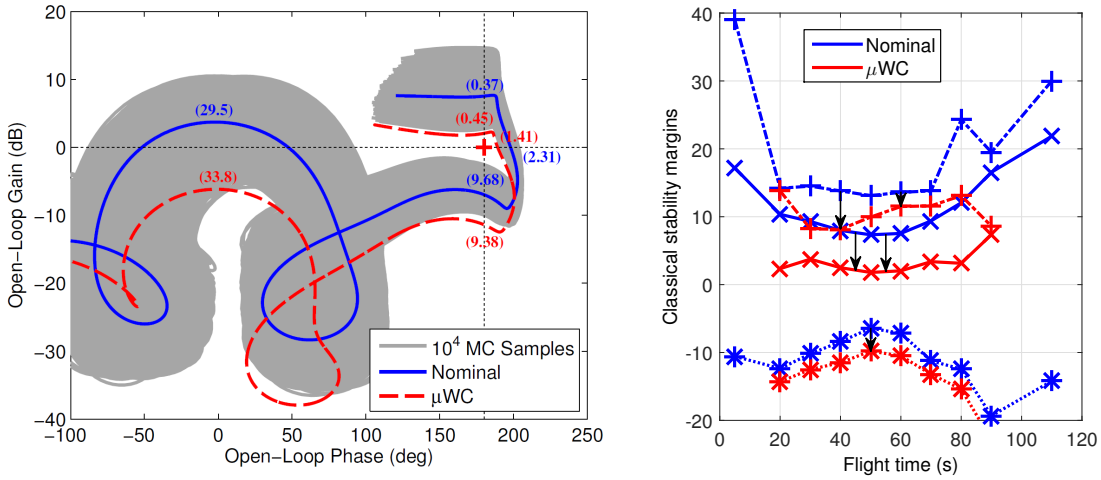

(a) Comparison of Nichols charts $\psi_{\mathrm{INS}}(s)/\psi_{e}(s)$ at t=60 s (frequencies in rad/s at critical points shown inside brackets)

(b) Comparison of RB stability margins (against Fig. 12b)

Fig. 15 Nominal and worst-case stability indicators

Figure 15a also shows the response with 10000 Monte Carlo (MC) random LFT samples. These results clarify the effectiveness of the μ algorithm which, in a single shot, was able to identify conditions for a more intense degradation of stability. Therefore, μ analysis can also be employed to complement MC campaigns by narrowing the parameter sampling around the critical areas identified by μ. These WC margins are very realistic in the sense that they are derived form the lower bound peak of μ and, since the actual value of μ lies somewhere between its lower and upper bounds, even worse stability conditions may be attained in practice. Nonetheless, it must be understood that μ analysis is an inherently conservative methodology and the worst-cases found are generated by extremely unlikely configurations.

V. Robust Performance Assessment

The RS analysis introduced in the previous section can be further extended to directly assess how system performance is affected by uncertainties. This section shows how the robust performance (RP) problem is reshaped as a RS problem and how the considerations extracted in the frequency domain with μ are translated into the actual response of the system throughout the flight. Comparative results are shown between pre and post-flight assessments of VEGA.

A. Performance μ analysis

As shown in Subsection III A, RS is based on the size (i.e., norm) of the transfer functions from $\mathbf{w}_\mathrm{p}$ to $\mathbf{z}_\mathrm{p}$ in the face of all the plants in the uncertainty set. For the RP test, the signals $\mathbf{d}_\mathrm{p}$ and $\mathbf{e}_\mathrm{p}$ are scaled to one (into $\mathbf{d}'_\mathrm{p}$ and $\mathbf{e}'_\mathrm{p}$, respectively) for ease of conditioning and the assessment is carried out with respect to the relationship between them. The normalization is chosen so that all the performance requirements are met if:

$$||\mathbf{e}'_\mathrm{p}(\mathrm{s})\mathbf{d}'^{-1}_\mathrm{p}(\mathrm{s})||_\infty < 1, \qquad \forall \Delta_\mathrm{u}(\mathrm{s}) : ||\Delta_\mathrm{u}(\mathrm{s})||_\infty \leq 1 \tag{36}$$

The evaluation of this condition is equivalent to the application of μ to the system of Fig. 16, where the uncertainty structure is given by $\Delta_\mathrm{RP}(\mathrm{s}) = \mathrm{diag}\left(\Delta_\mathrm{u}(\mathrm{s}), \Delta_\mathrm{p}(\mathrm{s})\right)$ and $\Delta_\mathrm{p}(\mathrm{s})$ is a fictitious full complex perturbation closing the performance specification. Formulating the system as in Fig. 16, where $N(\mathrm{s})$ represents $M(\mathrm{s})$ with weighted inputs and outputs for the referred normalization, the performance specifications of $\mathcal{F}_\mathrm{u}\left\{N(\mathrm{s}),\, \Delta_\mathrm{u}(\mathrm{s})\right\}$ are met over all allowable uncertain elements if and only if [12, 14]:

$$\mu_{\Delta_\mathrm{RP}}\left(N(j\omega)\right) < 1, \quad \forall\, \omega \in \mathbb{R} \tag{37}$$

As mentioned above, the input and output signals are normalized. Input scaling is based upon the expected maximum value, assumed to be 1 deg for the commanded attitude angle and 3 for the unitary noise wind signal (providing a 3 standard deviation coverage of the filters derived in Subsection II E). Therefore, the input weight is $W_\mathrm{d}(\mathrm{s}) = \mathrm{diag}(\pi/180,\ 3)$. In terms of system performance requirements, specifications are typically provided through a bound $F(\mathrm{s})$ such that $|\mathbf{e}_\mathrm{p}(\mathrm{s})\mathbf{d}'^{-1}_\mathrm{p}(\mathrm{s})| < |F(\mathrm{s})|$ and $F(\mathrm{s}) = W_\mathrm{e}^{-1}(\mathrm{s})$ [21]. The former condition is thus ensured if RP is verified because $|W_\mathrm{e}(\mathrm{s})\mathbf{e}_\mathrm{p}(\mathrm{s})\mathbf{d}'^{-1}_\mathrm{p}(\mathrm{s})| = |\mathbf{e}'_\mathrm{p}(\mathrm{s})\mathbf{d}'^{-1}_\mathrm{p}(\mathrm{s})| < 1$.

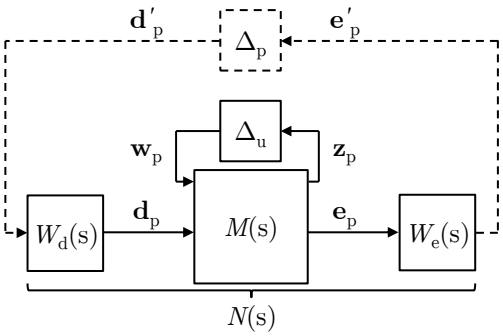

Fig. 16 Block diagram of the LFT model for robust performance analysis

In the present case, four output weights are used to highlight the effects associated to different indicators, as shown in Table 2. These indicators are based on the output vector $\mathbf{e}_{\mathrm{p}}(\mathrm{s})$ of Fig. 10 and, although not providing a direct reflection of all the requirements of VEGA in atmospheric flight, were selected to represent the most interesting interactions from Subsection II F. Note also that the weights vary with the time of flight.

The μ analysis results for the four indicators, one at a time, again at t=60 s, are summarized in Fig. 17. It shows the bounds of μ over the frequency, as well as the most significant perturbations composing the $\Delta_{\mathrm{u_{critic}}}(\mathrm{s})$ that corresponds to the μ peaks, with [-1,1] ranging from minimum to maximum uncertainty level. The comparison between RP and RS (Fig. 14) is also provided.

The first observation is related to the RS perturbations. The size of each individual uncertainty tends to be slightly below unity, as the peak of the μ lower bound is slightly larger than one. Furthermore, the overall combination of uncertainties allows to retrieve the physical meaning of the results. In fact, the WC is achieved by favoring the aerodynamic moment of the LV μ_α (Eq. (4)), increasing Q, C_{N_α} and x_{CP}, in detriment of its controllability μ_{c} (Eq. (5)), decreasing T and x_{CG}.

Conclusions on RP arise then as an additional result to RS, as indicated by Eq. (20). More specifically, μ bounds of RP are always larger or equal than those of RS (Fig. 17a) and, conversely, critical uncertainty sizes for RP are never larger than for RS (Fig. 17b). The result of the $\dot{z}$ indicator (uppermost plots), with which RS and RP bounds and uncertainties are practically coincident, is a good example where most degradation is caused by the lack of RS, while only a small contribution is introduced with the RP specification.

Table 2 Definition of weights for the performance analysis

Indicator	Performance weight	Justification
$\dot{z}$	$W_{\mathrm{e}} = \begin{bmatrix} 0 & (\dot{z}_{\mathrm{MAX}} - \dot{z}_{\mathrm{NOM}})^{-1} & 0\ 0\ 0 \end{bmatrix}$	Req. F3: Constant limitation of the lateral drift rate.
$Q\alpha$	$W_{\mathrm{e}} = \frac{180}{\pi} \begin{bmatrix} 0\ 0\ 0\ 0 & (Q\alpha_{\mathrm{MAX}} - Q\alpha_{\mathrm{NOM}})^{-1} \end{bmatrix}$	Req. F3: Constant limitation of the aerodyn. load.
β	$W_{\mathrm{e}} = \frac{180}{\pi} \begin{bmatrix} 0\ 0\ 0 & \left(\beta_{\mathrm{MAX}} \frac{\omega_{\mathrm{BW}}}{\mathrm{s} + \omega_{\mathrm{BW}}}\right)^{-1} & 0 \end{bmatrix}$	Req. F4: First-order limitation of the TVC deflection and bandwidth.
ψ_{e}	$W_{\mathrm{e}} = \frac{180}{\pi} \begin{bmatrix} 0\ 0 & \left.\frac{\psi_{\mathrm{e}}(s)}{\psi_{\mathrm{c}}(s)}\right\|_{\mathrm{ideal}}^{-1} & 0\ 0 \end{bmatrix}$	Req. F2/F5: Limitation of the tracking error by the sensitivity function with no parasitic effects (Fig. 11).

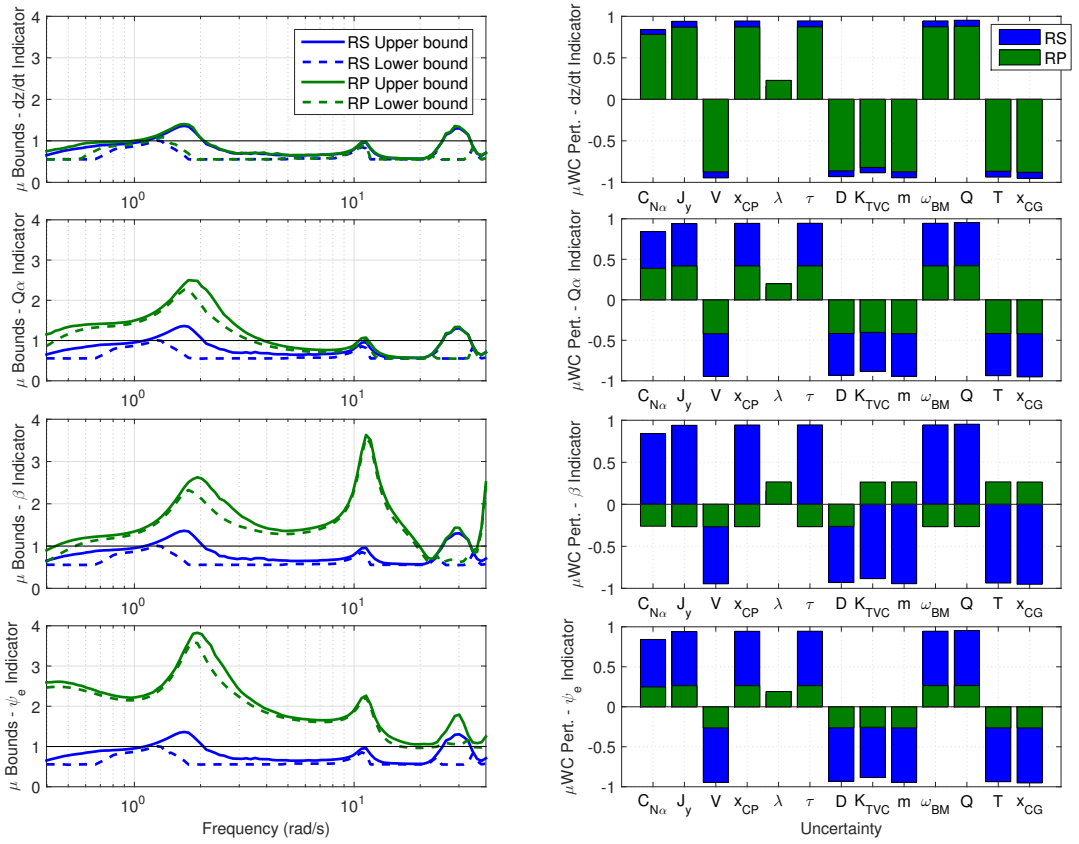

(a) RS and RP μ bounds (RS is the same for all indicators)

(b) WC RS and RP perturbations (RS is the same for all indicators)

Fig. 17 Robust performance results for each indicator of Table 2 at t=60 s

Nevertheless, a more significant RP degradation is introduced on the $Q\alpha$ indicator, with the corresponding decrease of the uncertainty sizes. As the effect of $Q\alpha$ is a characteristic of the RB

motion, it is only verified for low frequencies. On the other hand, the effect of the β indicator is more evident at higher frequencies due to the interaction between the HF modes and the bandwidth of the TVC. It is also interesting to notice that, as the RS and RP peaks of μ occur at different frequency regions, the uncertainty combinations that characterise them are also completely different.

Finally, a more intense effect throughout all the frequencies shows up with the ψ_e indicator. This observation was already expected since the ideal sensitivity function, which is given as performance specification, is degraded with a factor of three due to drift control and BM filters (Subsection III B). A significantly larger degradation is also achieved if all the indicators are assessed simultaneously.

B. High-fidelity time domain validation

In order to validate the results obtained in the previous subsection, the μWC configurations (derived with the μ algorithm) are tested in the nonlinear 6 degrees-of-freedom time domain simulator of VEGA atmospheric flight [9, 11]. In other words, the $\Delta_{u_{critic}}(s)$ from Fig. 17b, at t=60 s (Mach 2.6) for each performance indicator, were injected in the simulator and kept constant throughout the flight. All the remaining parameters of the simulator (e.g., thrust/sensor misalignments, actuator backlash, etc.), which are not captured in the LFT model (Eq. (20)) are set to nominal. In addition, only parameters associated to the rotation around the LV y-axis (from the bi-dimensional linear model) are perturbed.

Furthermore, as the underlying mission to the whole analysis already took place, the results obtained are inclusively checked against the corresponding flight data. The availability of flight data provides undoubtedly an additional level of insight into the problem and has been employed for the estimation of some of its parameters. For example, the nominal value and production uncertainties of the BM frequencies assumed in the μ analysis are derived from the successive flights of VEGA. In addition, for a meaningful matching between simulation and flight results, the estimated wind profile and roll motion are also included in the simulations.

The outcomes are compared between nominal (all the uncertainties are zero), μWC configurations and the actual VV05 flight [20]. Focusing on the drift response (Fig. 18a), degradation is evident upon the injection of the WC uncertainties, essentially concerning drift variation rather than its norm (recall that the RP indicator is drift rate).

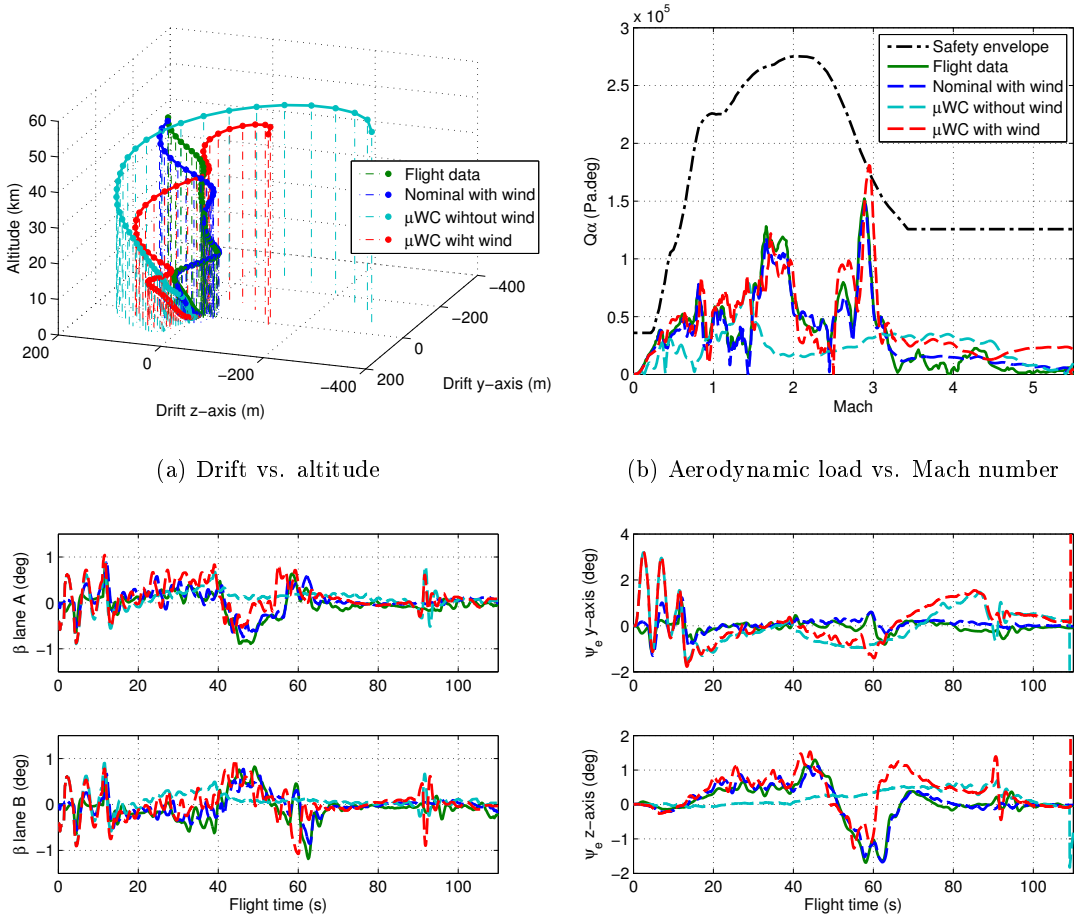

(a) Drift vs. altitude

(b) Aerodynamic load vs. Mach number

(c) TVC Actuation vs. time

(d) Attitude error vs. time

Fig. 18 Nominal, worst-case and actual flight responses, with and without wind

The evolution of the aerodynamic load indicator is then illustrated in Fig. 18b. This figure clearly demonstrates that the wind plays a critical role in the overall trend in terms of aerodynamic load, thus every worst-case is extremely wind-dependent. The nominal simulation is actually very representative of the flight results, showing only slight differences due to dispersions of the real system. However, under μWC conditions, a noticeable load peak is observed around Mach 3, which falls outside of the safety envelope. This means that, even with an LFT model that covers a smaller set of uncertainties than the high-fidelity simulator, μ analysis was able to effectively identify a realistic combination of parameters for which the system requirements are not satisfied. In practice, with all the uncertainties that can be encountered, worse load peaks may yet be attained.

Analogous judgements can be made for TVC deflections and attitude errors, Fig. 18c and Fig. 18d, with more intense oscillations visible in the WC responses than during the flight.

VI. Conclusions

This paper demonstrates on an industrial launcher application the versatility of the structured singular value μ for dynamical systems robustness analysis. The VEGA launcher motion dynamics and its perturbations throughout atmospheric flight have been reformulated in a linear fractional transformation (LFT) fashion in order to capture the operational flight envelope and its deviations.

It has been shown that μ analysis is generally applicable, independently of the control system methods employed for design. This application addresses a gain-scheduled flight thrust vector control (TVC) system designed by means of classical and parameter optimization techniques. The μ robust stability analysis provides a frequency-wise insight on classical stability margins degradations in the face of structured perturbations that originate from non-reducible production of uncertainties. At each frequency, the critical combination of launcher parameter deviations is returned and, when implemented, reveals the physics of the degradation mechanism at system level. Throughout the flight envelope, worst-case parameter combinations are derived by freezing the system and executing local μ tests at discrete time instants. Worst-case conditions have been recovered over the entire atmospheric flight and submitted to detailed analysis in maximum dynamic pressure conditions.

Beyond the applicability of robust stability analysis, performance robustness requirements related to maximum wind drift, $Q\alpha$, control effort and attitude tracking are all assessed in the same way. This is done through appropriate matrix augmentation of the stability robustness problem. The results obtained provide a clear insight on the anatomy of performance degradation mechanisms over the various input/output channels of interest. Therefore, the μ methodology is particularly useful as a complement for the analyst engineer to traditional random sampling verification and validation techniques, narrowing down his search towards specific worst-case performance conditions with associated parameter combinations.

Finally, modeling assumptions and robust performance properties have been validated through comparative pre and post-flight analyses, which revealed to be globally coherent over the flight envelope. The meaningfulness of the proposed analysis strongly relies on the numerical quality of the modeling approach undertaken. LFT modeling choices in order to properly capture the relevant physical phenomena at hand are not arbitrary, especially in tight spectral regions where the

dynamical interplay over uncertainty degradation mechanisms is sensitive. It has been experienced that large-scale problems can be handled provided that the uncertainty vector remains reasonable in size. This is to ensure that meaningful lower/upper bound gaps are achieved from μ calculations. Numerical conditioning of the analysis problem has also a large influence. Besides employing scaling and conditioning techniques, system aggregation and integration must be treated with care.

The launcher uncertainty modeling has room for improvement, being subject to ongoing research. Most importantly, pitch/yaw coupling effects due to roll motion are being included, while the correlation of physically-related uncertain parameters (e.g., thrust and dynamic pressure) and the global time-parametrization of the LFT system will be further exploited.

Acknowledgements

The authors would like to acknowledge the recommendations and technical assistance provided by the VEGA Integrated Project Team (IPT) and the ESTEC Guidance, Navigation and Control (GNC) Section, in particular to Dr. G. Ortega. This work has been carried out under a traineeship grant supported by the Portuguese Foundation for Science and Technology (FCT).

References

[1] Stein, G., "Respect the Unstable", *IEEE Control Systems Magazine*, August 2003, pp. 12-25.

[2] Ruth, M., Lebsock, K. and Dennehy, C., "What's New is What's Old: Use of Bode's Integral Theorem to Provide Inside for 21st Century Spacecraft Attitude Control System Design Tuning," *AIAA Guidance, Navigation, and Control Conference*, 2-5 Aug. 2010, Toronto, Canada.

[3] Whorton, M., Yang, L. and Hall, R., "Similarity Metrics for Closed-Loop Dynamic Systems," *AIAA Guidance, Navigation, and Control Conference*, 18-21 Aug. 2008, Honolulu, Hawaii.

[4] Orr, J., VanZwieten, T., Wall, J. and Hall, C., "Space Launch System Ascent Flight Control Design," *AAS Guidance, Navigation, and Control Conference*, 31 Jan.-5 Feb. 2014, Breckenridge, CO.

[5] Hanson, J. and Beard, B., "Applying Monte Carlo Simulation to Launch Vehicle Design and Verification," *AIAA Guidance, Navigation, and Control Conference*, 2-5 Aug. 2010, Toronto, Canada.

[6] Valli, M., Spallota, D., Roux, C., Marcos, A., Mujumdar, A., Menon, P. and Bennani, S., "Thrust Vector Control Validation Results for Performance and Stability Robustness Assessment," *3rd CEAS Conference on Guidance, Navigation, and Control*, 13-15 Apr. 2015, Toulouse, France.

[7] Doyle, J., Francis, B. and Tannenbaum, A., "Feedback Control Theory," *Macmillan Publishing*, 1990.

[8] Menon, P. P., Bates, D.G. and Postlethwaite, I., "Nonlinear Robustness Analysis of Flight Control Laws for Highly Augmented Aircraft," *Control Engineering Practice*, Vol. 15, No. 6, 2007, pp. 655-662.

[9] Marcos, A., Marina, H., Mantini, V., Roux, C. and Bennani, S., "Optimization-based Worst-case Analysis of a Launcher during the Atmospheric Ascent Phase," *AIAA Guidance, Navigation, and Control Conference*, 19-22 Aug. 2013, Boston, MA.

[10] Shin, J.-Y., Balas, G. and Packard, A., "Worst-case Analysis of the X-38 Crew Return Vehicle Flight Control System," *AIAA Journal of Guidance, Control, and Dynamics*, Vol. 24, No. 2, 2001, pp. 261-269.

[11] Marcos, A., Rosa, P., Roux, C., Bartolini, M. and Bennani, S., "An Overview of the RFCS Project V&V Framework: Optimization-based and Linear Tools for Worst-case Search," *CEAS Space Journal*, Vol. 7, No. 2, 2015, pp. 303-318.

[12] Stein, G. and Doyle, J., "Beyond Singular Values and Loop Shapes," *AIAA Journal of Guidance, Control, and Dynamics*, Vol. 14, No. 1, 1991, pp. 5-16.

[13] Doyle, J., Packard, A. and Zhou, K., "Review of LFTs, LMIs, and μ," *30th IEEE Conference on Decision and Control*, 11-13 Dec. 1991, Brighton, England.

[14] Zhou, K., Doyle, J. and Glover, K., "Robust and Optimal Control," *Prentice Hall*, 1995.

[15] Enns, D., "Rocket Stabilization as a Structured Singular Value Synthesis Design Example," *IEEE Control Systems*, Vol. 11, No. 4, 1991, pp. 67-73.

[16] Balas, G. and Packard, A., "Design of Robust, Time-varying Controllers for Missile Autopilots," *1st IEEE Conference on Control Applications*, 13-16 Sep. 1992, Dayton, OH.

[17] deVirgilio, M. A. and Kamimoto, D. K., "Practical Applications of Modern Controls for Booster Autopilot Design," *12th AIAA Digital Avionics Systems Conference*, 25-28 Oct. 1993, Fort Worth, TX.

[18] Ganet-Schoeller, M., "Towards Structured $\mathcal{H}_\infty$ Synthesis for Flexible Launcher," *3rd CEAS Conference on Guidance, Navigation, and Control*, 13-15 Apr. 2015, Toulouse, France.

[19] Roux, C. and Cruciani, I., "Scheduling Schemes and Control Law Robustness in Atmospheric Flight of VEGA Launcher," *7th ESA GNC Conference*, 1-5 Jun. 2008, Tralee, Ireland.

[20] Arianespace, "VEGA VV05 Launch Kit," 22 Jun. 2015, available at `http://arianespace.com/news-launch-kits/launch-kit.asp`.

[21] Gu, D.-W., Petkov, P. and Konstantinov, M. M., "Robust Control Design with MATLAB," *Springer-Verlag London*, 2013.

[22] Greensite, A. L., "Analysis and Design of Space Vehicle Flight Control Systems," *Spartan Books*, 1970.

[23] Suzuki, H., "Load Relief Control of H-IIA Launch Vehicle," *16th IFAC Symposium on Automatic Control in Aerospace*, 14-18 Jun. 2004, Saint-Petersburg, Russia.

[24] Wie, B., Du, W. and Whorton, M., "Analysis and Design of Launch Vehicle Flight Control Systems," *AIAA Guidance, Navigation, and Control Conference*, 18-21 Aug. 2008, Honolulu, Hawaii.

[25] Orr, J., Johnson, M., Wetherbee, J. and McDuffie, J., "State Space Implementation of Linear Perturbation Dynamics Equations for Flexible Launch Vehicles," *AIAA Guidance, Navigation, and Control Conference*, 10-13 Aug. 2009, Chicago, IL.

[26] Andrews, C. D., "Terrestrial Environment (Climatic) Criteria Guidelines for Use in Aerospace Vehicle Development," *NASA Technical Memorandum 4511*, 1993.

[27] Marcos, A. and Bennani, S., "LPV Modeling, Analysis and Design in Space Systems: Rationale, Objectives and Limitations," *AIAA Guidance, Navigation, and Control Conference*, 10-13 Aug. 2009, Chicago, IL.